Journal of Sound and Vibration 329 (2010) 3149–3170

Contents lists available at ScienceDirect

Journal of Sound and Vibration

journal homepage: www.elsevier.com/locate/jsvi

Dynamic stability of a base-excited thin orthotropic cylindrical shell with top mass: Simulations and experiments ☆

N.J. Mallon [a], R.H.B. Fey [b,*], H. Nijmeijer [b]

[a] TNO Built Environment and Geosciences, Centre for Mechanical and Maritime Structures, PO Box 49, 2600 AA Delft, The Netherlands
[b] Eindhoven University of Technology, Department of Mechanical Engineering, PO Box 513, 5600 MB Eindhoven, The Netherlands

ARTICLE INFO

Article history:
Received 3 April 2009
Received in revised form
11 January 2010
Accepted 3 February 2010
Handling Editor: M.P. Cartmell
Available online 25 February 2010

ABSTRACT

Considering both an experimental and a numerical approach, the dynamic stability of a harmonically base-excited thin orthotropic cylindrical shell carrying a top mass is examined. To be able to compare the experimentally obtained results with numerical results, a semi-analytical coupled shaker-structure model is derived. Using the semi-analytical model, it is shown that the dynamic stability analysis of the base-excited cylindrical shell with top mass should be concentrated near a low frequency resonance, corresponding to a mode, in which axial vibrations of the (cylindrical shell with) top mass dominate. In this frequency region, the shell may exhibit an aperiodic beating type of response, if some critical value of the amplitude of the harmonic base-excitation is exceeded. This beating response is characterized by severe out-of-plane deformations. The experimental results qualitatively confirm the numerical observations.

1. Introduction

In the field of dynamic stability of structures, the research regarding cylindrical shells subjected to a harmonic excitation in axial direction encompasses a large and significant part of the present literature, see [1–4] and references cited therein. The majority of these analyses consider parametric instabilities of bare cylindrical shells, i.e. axi-asymmetrical vibration modes are excited through a *Mathieu* type of instability. In practise, a cylindrical shell is often employed as a support structure for carrying a substantial top mass. In this case, a relatively low frequency resonance, corresponding to a vibration mode dominated by axial displacements of the (cylindrical shell with) top mass, i.e. a kind of suspension mode, is introduced.

In [5], it is shown that for the case of a top mass, which can only move in vertical direction, the dynamic stability limits of the harmonically, axially excited cylindrical shell are no longer dictated by parametric instabilities in the high frequency range (near excitation frequencies equal to two times the eigenfrequency of an axi-asymmetrical vibration mode). Instead, the dynamic stability limits are now found in the top of a low frequency resonance far below the parametric instability regions, corresponding to the suspension mode introduced in the previous paragraph. To be more specific, by increasing the amplitude of the prescribed base-acceleration, the harmonic response may become unstable in the resonance peak, and a beating type of response with severe (undesired) out-of-plane deformations of the cylindrical shell may appear instead. Furthermore and similar to the case of static buckling of axially compressed cylindrical shells, it is illustrated in [5] that the

☆ This research is supported by the Dutch Technology Foundation STW, applied science division of NWO and the technology programme of the Ministry of Economic Affairs (STW project EWO.5792).

* Corresponding author. Tel.: +31 40 247 5406; fax: +31 40 246 1418.
E-mail address: R.H.B.Fey@tue.nl (R.H.B. Fey).

0022-460X/$ - see front matter © 2010 Elsevier Ltd. All rights reserved.
doi:10.1016/j.jsv.2010.02.007

critical value for the amplitude of the prescribed harmonic base-acceleration, for which the harmonic response changes to the severe post-critical response, highly depends on the initial imperfections present in the shell.

The objective of this paper is to validate these results. Hereto, experimental results for a base-excited thin cylindrical shell with top mass will be presented and a comparison with semi-analytical results will be made. At the experimental setup used, the base-excitation is realized by supplying a harmonic input voltage to an electrodynamic shaker system. For this case the resulting base acceleration will not be purely harmonic, will not have a constant amplitude, but will be determined by the dynamics of the shaker system carrying the thin cylindrical shell with top mass. In addition, the bare shaker table has a low axial stiffness and a relatively high damping, due to the effect of back-voltage. If the cylindrical shell with top mass is fixed on the shaker table, the shaker-shell-top mass structure exhibits two low frequency resonances (low frequency compared to resonance frequencies corresponding to axi-asymmetrical modes of the cylindrical shell). The vibration mode corresponding to the first resonance is dominated by the axial displacements of the shaker table. The vibration mode corresponding to the second resonance is dominated by axial displacements of the (cylindrical shell with) top mass. This mode has some coupling with the heavily damped shaker table motion resulting in some additional damping. If one would neglect the shaker dynamics and would consider a prescribed harmonic base-acceleration instead, as considered in [5], the first resonance would disappear, whereas the resonance frequency of the suspension mode of the top mass would shift to a lower frequency and would become less damped. From the discussion above, it will be clear that results obtained by voltage excitation can only be compared in a qualitative sense with results obtained by a prescribed harmonic base-acceleration, as considered in [5]. Therefore, to enable quantitative comparison between experimental results and semi-analytical results in the current paper, the semi-analytical model of the base-excited cylindrical shell with top mass will be coupled to a model of the electrodynamic shaker. Furthermore, the cylindrical shell made from Poly Ethylene Terephthalate appeared to behave orthotropic in the elastic domain. Therefore, in the current paper orthotropic material behaviour will be introduced in the semi-analytical modelling approach developed in [5] for isotropic cylindrical shells.

Experimental results considering a base-excited cylindrical shell with a free top mass, i.e. the top mass is only supported by the cylindrical shell, are presented in [6]. Near the resonance of the first axi-symmetric vibration mode, a very severe unstationary response is found. In this region, the base-acceleration due to the shaker could not be controlled to remain purely harmonic. Furthermore, the obtained results could not be explained using numerical simulations. Consequently, a combined numerical and experimental analysis of a base-excited cylindrical shell carrying a top mass, as will be presented in this paper, has not been previously presented.

The outline for this paper is as follows. In the next section, the experimental setup of the cylindrical shell with top mass will be introduced and the material properties of the cylindrical shell will be determined. In Section 3, the coupled shaker-structure model will be discussed. In Section 4, modal analysis and static buckling analysis will be performed and results will be compared with finite element analysis (FEA) results. The theoretical modal analysis results will be compared with experimental results. Dynamic stability of the cylindrical shell with top mass excited by the shaker will be studied numerically in Section 5 and experimentally in Section 6. Finally, in Section 7 conclusions will be presented.

2. Experimental setup

The seamless cylindrical shell, which is used for the experiments, is cut out from an unused beverage bottle made of Poly Ethylene Terephthalate (PET), see Fig. 1. The obtained cylindrical shell has radius R (measured at the neutral plane) and (average) thickness h. The shell thickness varies in axial direction by approximately 2 percent. The PET bottle is produced by using a blow moulding technique. During this process, the material is stretched in the axial direction of the bottle and subsequently in the circumferential direction of the bottle. Since this biaxial stretching is performed with different stretch ratios in the two (perpendicular) directions, a directional dependency of the elasticity properties is introduced. The elasticity properties of a biaxially stretched, thin PET film may fairly well be approximated using an orthotropic symmetric material description, with principle directions aligned with the two stretch directions [7]. This approximation is also used here to model the elasticity properties of the PET cylindrical shell. More specifically, the shell is assumed to be made of orthotropic material with principle directions e_1 and e_2 coinciding with, respectively, the axial coordinate x and the circumferential coordinate θ (i.e. the two stretch directions), see Fig. 1. The orthotropic shell material model is described by four parameters, i.e. Young's moduli in x and θ direction (E_x and E_θ), the shear modulus $G_{x\theta}$, and one Poisson's ratio (either ν_x or ν_θ, since $\nu_\theta E_x = \nu_x E_\theta$). The procedure followed to identify these parameters is discussed in detail in [8]. The resulting material and geometrical parameter values are listed in Table 1.

Since the in-plane boundary conditions have a significant influence on the thin shell behaviour [9–11], special effort is taken to obtain a rigid clamping of the cylindrical edges. An exploded view of the construction used to clamp edges of the cylindrical shell is depicted in Fig. 2. The cylindrical shell edge is fixed between an inner ring, which fits exactly to the inner diameter of the shell, and an open ring with conical outer shape. The outer ring, which has a conical inner shape, is screwed over the open ring on the inner ring. In this manner, the open ring is compressed radially on the cylindrical shell surface, resulting in a stiff circle line contact between the clamping rings and the thin shell. Air outlets at the bottom clamping structure avoid entrapment of air in the shell.

The experimental setup is depicted in Fig. 3. The thin cylindrical shell, which is fixed between clamping rings both at its top and at its bottom, is mounted between two linear sledges with very low friction in axial direction, see Fig. 3. At the top

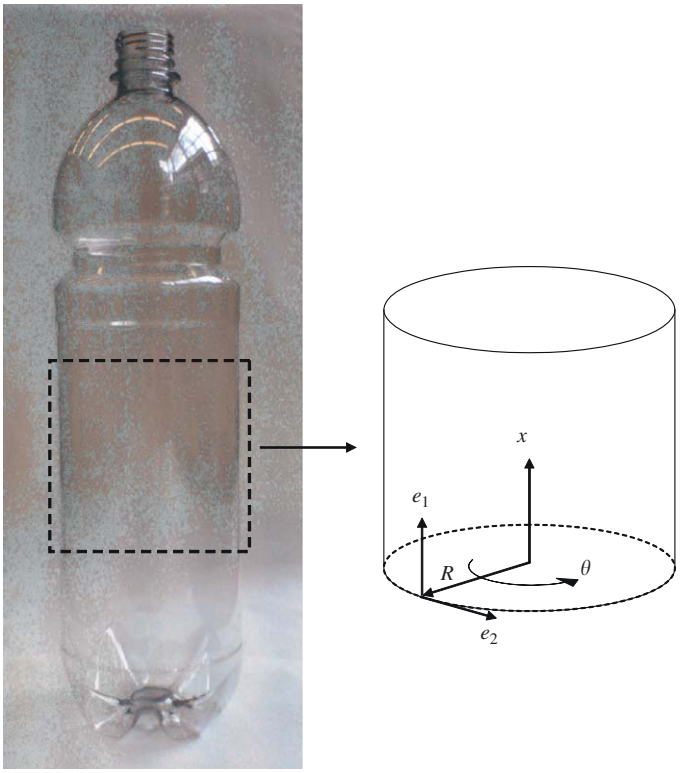

Fig. 1. Cylindrical shell from PET beverage bottle.

Table 1
Material and geometrical properties of the orthotropic cylindrical shell.

E_x	3.85	(GPa)	E_θ	6.00	(GPa)	$G_{x\theta}$	1.94	(GPa)
v_x	0.25	(–)	v_θ	0.39	(–)	ρ	1350	(kg/m^3)
L	85	(mm)	R	44	(mm)	h	0.23	(mm) (R/h=191)

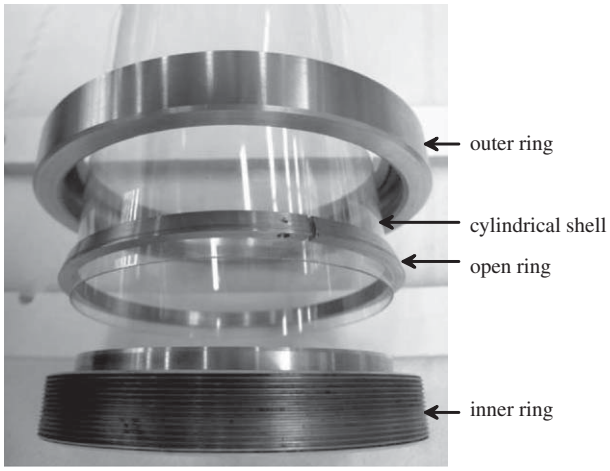

Fig. 2. Exploded view of one clamping ring for cylindrical shell.

side, the linear sledge is based on air bearings. At the bottom side, the linear sledge is realized by an elastic mechanism based on elastic leaf springs. The purpose of these support mechanisms is to minimize transversal motions and rotations of the cylindrical shell edges. The upper linear sledge and upper clamping structure actually act as the rigid top mass (total

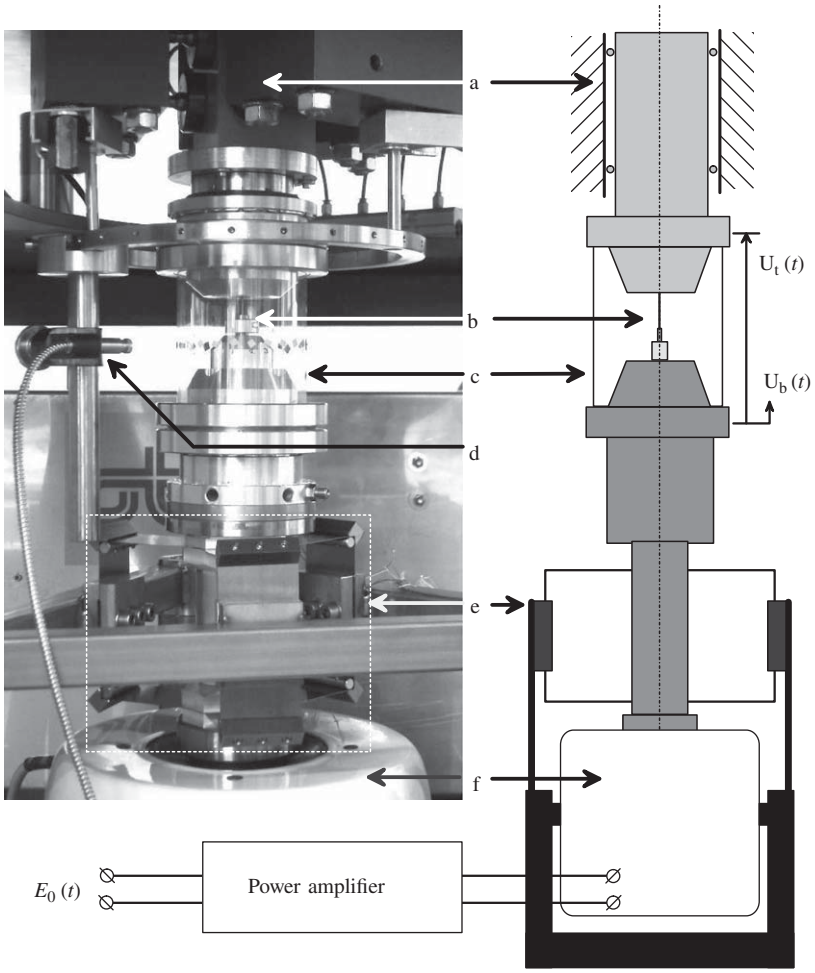

Fig. 3. Picture and schematic overview of the experimental setup ((a) top linear sledge based on air bearings, (b) linear variable differential transformer (LVDT), (c) cylindrical shell, (d) laser vibrometer, (e) bottom elastic support mechanism, (f) electrodynamic shaker).

mass m_t=4.7 kg). The moving mass of the lower linear sledge, including the mass of the bottom clamping structure and the mass of the shaker armature, equals m_b=4.1 kg.

The axial base-excitation is realized using an electrodynamic shaker system (type LDS PA1000L/LDS V455), see Fig. 3. A periodic excitation is introduced by supplying a harmonically varying input voltage

$$E_0(t) = v_d \sin(2\pi f t)\,[\mathrm{V}], \tag{1}$$

to the power amplifier, which output voltage is supplied to the shaker. The amplifier works in a voltage mode of operation, i.e. the output voltage of the amplifier is kept proportional to its input voltage. No active feedback is used to control the acceleration of the shaker armature $\ddot{\mathbf{U}}_\mathbf{b}$. Consequently, as stated before, the resulting acceleration of the shaker (and thus the effective axial force on the cylindrical shell with top mass) will not be proportional to Eq. (1), but will be determined by the dynamics of the electro-mechanical shaker system carrying the cylindrical shell with top mass.

For dynamic response measurements, two sensors are used. Firstly, the relative axial displacement of the top mass $\mathbf{U_t}(t)$, see Fig. 3, is measured using a Shaevitz 100 MHR linear variable differential transformer (LVDT). Furthermore, a laser vibrometer (Ono Sokki LV 1500) is used to measure the transversal velocity $\dot{w}$ at one point of the cylindrical shell. The signal of the laser vibrometer is numerically integrated to obtain measurements in terms of transversal displacements w. To avoid drift during the numerical integration, the measurement signal is filtered using a high-pass filter with a cut-off frequency of $f = 1.6$ Hz. The data-acquisition and input signal generation is performed using a laptop equipped with Matlab/Simulink in combination with a TUeDACS AQI [12]. The sample frequency used is 4 kHz.

3. Modelling approach

In this section, the equations of motion are derived for the thin orthotropic cylindrical shell carrying a rigid top mass m_t. Since the cylindrical shell is excited at its base in axial direction by an electrodynamic shaker, an electro-mechanical model

of the shaker will be included in the semi-analytical model, in order to be able to compare the experimental results with the semi-analytical results. The modelling of the orthotropic cylindrical shell with top mass is based on the same assumptions adopted in [5] for the modelling of an isotropic cylindrical shell with top mass.

3.1. Cylindrical shell model

The dimensions of the cylindrical shell are defined by the radius of the neutral plane R, thickness h, and length L. Considering the cylindrical coordinate system $[r=R,x,\theta]$ defined in Fig. 1, the axial in-plane displacement field is denoted by $u(t,x,\theta)$, the circumferential in-plane displacement field by $v(t,x,\theta)$, the radial out-of-plane displacement field by $w(t,x,\theta)$, and the radial imperfection shape by $w_0(x,\theta)$. For readability, the notations for the displacement fields and radial imperfection shape will be abbreviated to u, v, w, and w_0, respectively. The axial coordinate x and axial displacement field u are measured relative to the base-motion $\mathbf{U_b}\,(t)$.

According to *Donnell*'s assumptions, the nonlinear strain–displacement relations read [13,14]

$$\varepsilon_x = u_{,x}+\tfrac{1}{2}w_{,x}^2+w_{,x}w_{0,x},\quad \kappa_x=-w_{,xx},$$

$$\varepsilon_\theta=\frac{1}{R}(v_{,\theta}+w)+\frac{1}{2R^2}w_{,\theta}^2+\frac{1}{R^2}w_{,\theta}w_{0,\theta},\quad \kappa_\theta=-\frac{1}{R^2}w_{,\theta\theta},$$

$$\gamma_{x\theta}=\frac{1}{R}u_{,\theta}+v_{,x}+\frac{1}{R}(w_{,x}w_{,\theta}+w_{,x}w_{0,\theta}+w_{0,x}w_{,\theta}),\quad \kappa_{x\theta}=-\frac{1}{R}w_{,x\theta}, \tag{2}$$

where $_{,x}$ means $\partial/\partial x$ and $_{,\theta}$ means $\partial/\partial\theta$. Note that in Eq. (2), the radial displacement field w and the radial imperfection shape w_0 are measured positively inwards.

Considering orthotropic material properties with principle axes, which coincide with the cylindrical coordinate axes, the stress resultants and stress couples per unit length are defined by [15,16]

$$\begin{bmatrix}N_x\\N_\theta\\N_{x\theta}\end{bmatrix}=h\begin{bmatrix}C_{11}&C_{12}&0\\C_{21}&C_{22}&0\\0&0&C_{33}\end{bmatrix}\begin{bmatrix}\varepsilon_x\\\varepsilon_\theta\\\gamma_{x\theta}\end{bmatrix},\quad \begin{bmatrix}M_x\\M_\theta\\M_{x\theta}\end{bmatrix}=\frac{h^3}{12}\begin{bmatrix}C_{11}&C_{12}&0\\C_{21}&C_{22}&0\\0&0&C_{33}\end{bmatrix}\begin{bmatrix}\kappa_x\\\kappa_\theta\\\kappa_{x\theta}\end{bmatrix}, \tag{3}$$

where

$$C_{11}=\frac{E_x}{1-\nu_x\nu_\theta},\quad C_{22}=\frac{E_\theta}{1-\nu_x\nu_\theta},\quad C_{33}=G_{x\theta},\quad C_{12}=C_{21}=\nu_\theta\frac{E_x}{1-\nu_x\nu_\theta}. \tag{4}$$

The following boundary conditions for the cylindrical shell with rigid end-disks are considered ('–' means not prescribed)

	u	$u_{,\theta}$	v	w	M_x
$x=0$	0	0	0	0	0
$x=L$	–	0	0	0	0

(5)

Note that the base-motion does not appear in the boundary conditions, since u and x are measured relative to $\mathbf{U_b}(t)$. Indeed, for a thin cylindrical shell mounted between two rigid end-disks, the clamping condition (in practice) is probably closer to the condition $w_{,x}=0$ than to the condition $M_x=0$. Nevertheless, the clamping condition is assumed to be $M_x=0$, since this allows for a simple expansion of w. This assumption is supported by the fact, that previous studies show, that the rotational boundary condition ($M_x=0$ vs. $w_{,x}=0$) has only a mild influence on the eigenfrequencies [9,10], parametric instabilities [17], and nonlinear vibrations [10,11]. The boundary condition in terms of the membrane force N_x at $x=L$, due to the inertia force of the top mass, is not included. This force will be included via the kinetic energy.

The strain energy of the structure, corresponding to *Donnell*'s assumptions, reads as follows:

$$\mathcal{U}_s=\frac{1}{2}\int_0^{2\pi}\int_0^L(N_x\varepsilon_x+N_\theta\varepsilon_\theta+N_{x\theta}\gamma_{x\theta})\,\mathrm{d}x\,R\,\mathrm{d}\theta+\frac{1}{2}\int_0^{2\pi}\int_0^L(M_x\kappa_x+M_\theta\kappa_\theta+M_{x\theta}\kappa_{x\theta})\,\mathrm{d}x\,R\,\mathrm{d}\theta. \tag{6}$$

The case $m_t\gg m_{shell}$, where m_t is the top mass and m_{shell} is the mass of the shell, is considered. Therefore, the contribution of the mass of the shell is neglected in the gravitational potential energy of the structure

$$\mathcal{U}_g=m_tg(\mathbf{U_b}(t)+u(t,L,\theta)), \tag{7}$$

where g is the acceleration due to gravity. Furthermore, the influence of in-plane inertia of the shell is also neglected in the kinetic energy

$$\mathcal{T}_{cyl} = \frac{1}{2}\rho h \int_0^{2\pi}\int_0^{L} \dot{w}^2 \,\mathrm{d}x R\,\mathrm{d}\theta + \frac{1}{2} m_t \dot{u}_t^2, \tag{8}$$

where $\dot{u}_t = \dot{\mathbf{U}}_\mathbf{b}(t) + \dot{u}(t, L, \theta)$.

Based on Eqs. (6)–(8), the nonlinear equilibrium equations become

$$RN_{x,x} + N_{x\theta} = 0, \tag{9}$$

$$RN_{x\theta} + N_{\theta,\theta} = 0, \tag{10}$$

$$M_{x,xx} + \frac{2}{R}M_{x\theta,x\theta} + \frac{1}{R^2}M_{\theta,\theta\theta} + \frac{1}{R}N_\theta + N_x(w_{,xx} + w_{0,xx}) + \frac{2}{R}N_{x\theta}(w_{,x\theta} + w_{0,x\theta}) + \frac{1}{R^2}N_\theta(w_{,\theta\theta} + w_{0,\theta\theta}) = \rho h \ddot{w}. \tag{11}$$

Since the effects of in-plane inertia are neglected, these equations constitute a set of two static in-plane equilibrium equations (Eqs. (9)–(10)) and one dynamic out-of-plane equilibrium equation (Eq. (11)).

The out-of-plane displacement field is expanded as

$$w(t, x, \theta) = \sum_{i=1}^{N}\sum_{j=0}^{M} [\mathbf{Q}^{\mathbf{s}}_{\mathbf{ij}}(t)\sin(jn\theta) + \mathbf{Q}^{\mathbf{c}}_{\mathbf{ij}}(t)\cos(jn\theta)]\sin(\lambda_i x), \tag{12}$$

where $\lambda_i = i\pi/L$, i is the number of axial half-waves, n is the number of circumferential waves, and $\mathbf{Q}^{\mathbf{s,c}}_{\mathbf{ij}}(t)$ are $N(2M+1)$ generalized degrees of freedom (DOFs). Note that Eq. (12) exactly satisfies the boundary conditions for w, see Eq. (5). The N DOFs $\mathbf{Q}^{\mathbf{c}}_{\mathbf{i0}}(t)$ correspond to axi-symmetrical radial displacements and the $2NM$ DOFs $\mathbf{Q}^{\mathbf{s,c}}_{\mathbf{ij}}(t)$ ($j \neq 0$) to axi-asymmetrical displacement fields. The presence of pairs of companion modes (related to DOFs $\mathbf{Q}^{\mathbf{s}}_{\mathbf{ij}}$ and DOFs $\mathbf{Q}^{\mathbf{c}}_{\mathbf{ij}}$ for $j \neq 0$) with the same shape, but with a different angular orientation, is due to axi-symmetry of the (perfect) shell [2–4,18].

The following (axi-asymmetrical) expansion of the radial imperfection w_0 is considered

$$w_0(x, \theta) = h\sum_{i=1}^{N_e} e_i \sin(n\theta)\sin\left(\frac{i\pi x}{L}\right), \tag{13}$$

where $N_e \leq N$ and e_i are dimensionless imperfection amplitudes.

Using the above expressions for w and w_0, the in-plane equilibrium equations (Eqs. (9)–(10)) now consist of a set of linear coupled inhomogeneous partial differential equations (PDEs) in terms of u and v. In order to perform a reduction of the three independent displacement fields to one independent displacement field w, these two PDEs are solved symbolically. The solution procedure for this purpose is outlined in [8] and results in expressions for u and v, which are functions of w and w_0. These expressions exactly satisfy the in-plane equilibrium equations (Eqs. (9)–(10)) and the in-plane boundary conditions (Eq. (5)). During this step, an extra DOF $\mathbf{U_t}(t) = u(t, L, \theta)$ is introduced, which corresponds to the axial displacement of the top mass.

3.2. Shaker model

The linear model of the electrodynamic shaker is depicted in Fig. 4, where the electrical part and the mechanical part are presented separately. The electrical part of the model (Fig. 4(a)) is described by a power amplifier, current $I(t)$, coil resistance R, coil inductance L, current-to-force constant κ_c, and back voltage $E_{\text{back}}(t) = -\kappa_c \dot{\mathbf{U}}_\mathbf{b}$. The power amplifier works in a voltage-mode of operation. More specifically, in the frequency domain

$$E(\mathrm{j}\omega) = G_{\text{amp}}(\mathrm{j}\omega)E_0(\mathrm{j}\omega), \tag{14}$$

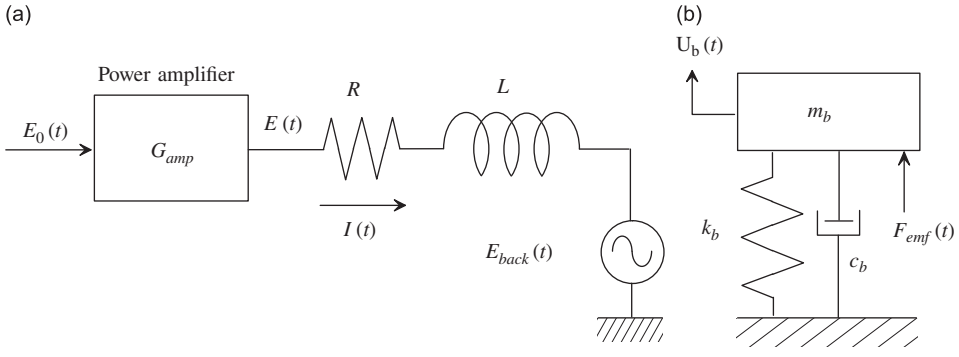

Fig. 4. Model of the electrodynamic shaker (electrical part (a), mechanical part (b)).

Table 2
Parameters of shaker model and amplifier model.

c_b	278	(kg/s)	L	2.6×10^{-3}	(H)	P_{amp}	-88.3	(–)
m_b	3.0	(kg)	κ_c	11.5	(N/A)	b_{amp}	1.4×10^{-3}	(s^{-1})
k_b	5.28×10^4	(N/m)	R	0.9	(Ω)			

where $G_{\text{amp}}(j\omega)$ (with $j^2 = -1$) is the frequency dependent amplifier gain, E the amplifier output voltage, and E_0 the amplifier input voltage.

Mass m_b of the mechanical part of the model (Fig. 4(b)) corresponds to the moving mass of the lower linear sledge, including the mass of the bottom clamping and the mass of the shaker armature, see Fig. 3. This mass, which is supported by an elastic suspension with stiffness k_b, is excited by the electromagnetic force $F_{\text{emf}}(t)=\kappa_c I(t)$. The vertical displacement of the mass is described by DOF $\mathbf{U_b}$. Energy dissipation in the mechanical part of the shaker is modelled by a linear viscous damping force with viscous damping constant c_b. It should be noted that the shaker base is assumed to be rigidly connected to the fixed world. If this assumption would not be valid, the mechanical part of the shaker model would need to be extended to a multi-DOF model, resulting in more mechanical parameters to be identified, see for example [19].

The dynamics of the shaker are now described by the following two coupled ordinary differential equations [20]

$$L\dot{I}+RI+\kappa_c\dot{\mathbf{U}}_\mathbf{b}=E(t),\quad m_b\ddot{\mathbf{U}}_\mathbf{b}+c_b\dot{\mathbf{U}}_\mathbf{b}+k_b\mathbf{U}_\mathbf{b}=\kappa_c I+F_{\text{str}}, \tag{15}$$

where E is related to E_0 by Eq. (14), and F_{str} is the force exerted to the shaker mass by the cylindrical shell with top mass. Force F_{str} in general depends on $\mathbf{Q}^{\mathbf{s,c}}_{\mathbf{ij}}(t)$, $\mathbf{U_t}(t)$, and first and second time derivatives of these DOFs. During the identification procedure of the unknown parameters of the excitation mechanism, in which the bare shaker was used, i.e. $F_{\text{str}}=0$ N, a frequency dependency of the amplifier gain defined by

$$G_{\text{amp}}(j\omega)=P_{\text{amp}}(b_{\text{amp}}\cdot j\omega+1) \tag{16}$$

is adopted to obtain a good fit of the combined shaker-amplifier dynamics for the frequency range of interest (0–300 Hz). The parameters of the combined shaker-amplifier model are identified using frequency domain techniques, see [8] for more details. The identified parameter values for the shaker model and the amplifier model are listed in Table 2. Note that using Eq. (16), the time domain version of Eq. (14) becomes $E(t)=P_{\text{amp}}(b_{\text{amp}}\dot{E}_0(t)+E_0(t))$, where E_0 is the known function of time given by Eq. (1). This time domain version will be used in the next subsection.

3.3. The coupled shaker-structure model

The coupled shaker-structure model will be derived by following a charge-displacement formulation of Lagrange's equations [21]. In this formulation, energy and work expressions of the coupled structure are formulated in terms of mechanical DOFs and, in this case, a single additional *charge* coordinate q, whose time derivative constitutes the current through the electrical part of the shaker model, i.e. $\dot{q}=I$.

The total set of $N(2M+1)+3$ DOFs of the coupled model is collected in the column

$$\mathbf{Q}^*=[\mathbf{Q^c_{10}},\ldots,\mathbf{Q^s_{NM}},\mathbf{Q^c_{NM}},\mathbf{U_t},\mathbf{U_b},q]^{\text{T}}, \tag{17}$$

where $\mathbf{Q^{s,c}_{ij}}$ and $\mathbf{U_t}$ are the generalized DOFs of the structure and $\mathbf{U_b}$ is the axial motion of the shaker (see Fig. 4).

Linear viscous damping is included in the cylindrical shell structure via the following Rayleigh dissipation function:

$$\mathcal{R}_{cyl}=\frac{1}{2}\sum_{i=1}^{N}\sum_{j=0}^{M}c_{ij}(\dot{\mathbf{Q}}^{\mathbf{c}}_{\mathbf{ij}})^2+\frac{1}{2}\sum_{i=1}^{N}\sum_{k=1}^{M}c_{ik}(\dot{\mathbf{Q}}^{\mathbf{s}}_{\mathbf{ik}})^2+\frac{1}{2}c_t\dot{\mathbf{U}}^2_{\mathbf{t}}, \tag{18}$$

where c_{ij}, c_{ik}, and c_t are positive constants. Furthermore, in the model of the cylindrical shell structure, the axial motions are defined with respect to an arbitrary base motion $\mathbf{U_b}$, see Eq. (8). For the coupled shaker-structure system, the energy and work expressions and the Rayleigh dissipation function now become as follows:

$$\begin{aligned}
\mathcal{M}&=\tfrac{1}{2}L\dot{q}^2+\kappa_c\dot{q}\mathbf{U_b},\\
\mathcal{T}&=\mathcal{T}_{\text{cyl}}+\tfrac{1}{2}m_b\dot{\mathbf{U}}^2_{\mathbf{b}},\\
\mathcal{V}&=\mathcal{U}_s+\mathcal{U}_g+\tfrac{1}{2}k_b\mathbf{U}^2_{\mathbf{b}},\\
\mathcal{R}&=\mathcal{R}_{\text{cyl}}+\tfrac{1}{2}c_b\dot{\mathbf{U}}^2_{\mathbf{b}}+\tfrac{1}{2}RI^2,\\
\delta\mathcal{W}_{\text{nc}}&=E(t)\delta q,
\end{aligned} \tag{19}$$

where $\mathcal{M}$ is the magnetic energy of the moving coil of the shaker, and $\delta\mathcal{W}_{\text{nc}}$ is the virtual work of $E(t)$ [21], which is the output voltage of the amplifier, see the previous subsection. Defining the Lagrangian $\mathcal{L}$ of the complete system by

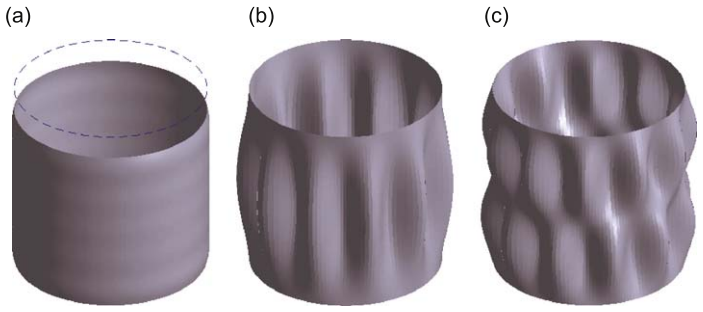

Fig. 5. Three types of vibration modes of cylindrical shell (top mass not shown).

$\mathcal{L}=\mathcal{T}+\mathcal{M}-\mathcal{V}$, the final coupled set of equations of motion can be determined by

$$\frac{\mathrm{d}}{\mathrm{d}t}\mathcal{L}_{,\dot{\mathbf{Q}}^*}-\mathcal{L}_{,\mathbf{Q}^*}+\mathcal{R}_{,\dot{\mathbf{Q}}^*}=\mathbf{b}E(t), \tag{20}$$

where $\mathbf{b}=[0,\ldots,0,1]^{\mathrm{T}}$ is an $N(2M+1)+3$ dimensional column. Among others, this will lead to an explicit expression for F_{str}, the force exerted to the shaker mass by the cylindrical shell with top mass, which was introduced in Eq. (15).

3.4. Selection of the number of DOFs

For the sake of brevity, only one specific expansion of w, see Eq. (12), will be considered. The specific expansion is obtained by deleting, i.e. setting to zero, a number of DOFs, corresponding to the expansion of w with $N=10$ and $M=2$. The deleted DOFs are DOFs $\mathbf{Q}^{\mathbf{s}}_{\mathbf{ij}}$, $^{\mathbf{c}}$ with $\mathbf{i}=2,4,\ldots,10$, which correspond to axial-asymmetrical radial displacements, and DOFs $\mathbf{Q}^{\mathbf{s}}_{\mathbf{i2}}$ and $\mathbf{Q}^{\mathbf{c}}_{\mathbf{i1}}$, which are companion modes of the kept (both axi-asymmetric and axial-symmetric) modes. More specifically, for the analyses described in this paper, the out-of-plane displacement field is expanded as follows:

$$w(t,x,\theta)=\sum_{i=1,3,\ldots,9}[\mathbf{Q}^{\mathbf{c}}_{\mathbf{i0}}(t)+\mathbf{Q}^{\mathbf{s}}_{\mathbf{i1}}(t)\sin(n\theta)+\mathbf{Q}^{\mathbf{c}}_{\mathbf{i2}}(t)\cos(2n\theta)]\sin(\lambda_i x). \tag{21}$$

Note that for the modes with $2n$ waves in circumferential direction, the modes with DOFs $\mathbf{Q}^{\mathbf{c}}_{\mathbf{i2}}$ are selected, since these modes are directly coupled (via a quadratic nonlinearity) to the modes with DOFs $\mathbf{Q}^{\mathbf{s}}_{\mathbf{i1}}$. The modes corresponding to (deleted) DOFs $\mathbf{Q}^{\mathbf{s}}_{\mathbf{i2}}$ would only posses a parametric coupling with the modes corresponding to DOFs $\mathbf{Q}^{\mathbf{s}}_{\mathbf{i1}}$.

The 15-DOF expansion of w given by Eq. (21) appears to be sufficient for accurately predicting the onset to the severe beating response, as was also found for the case of prescribed base-acceleration, see [5]. DOFs $\mathbf{Q}^{\mathbf{c}}_{\mathbf{i0}}$ correspond to modes being both axi-symmetric and axial-symmetric. The mode depicted in Fig. 5(a) is a linear combination of modes of this type and is therefore also both axi-symmetric and axial-symmetric itself. DOFs $\mathbf{Q}^{\mathbf{s}}_{\mathbf{i1}}$ and $\mathbf{Q}^{\mathbf{c}}_{\mathbf{i2}}$ correspond to modes being both axial-symmetric and axi-asymmetric, where DOFs $\mathbf{Q}^{\mathbf{c}}_{\mathbf{i2}}$ have a double number of circumferential waves compared to DOFs $\mathbf{Q}^{\mathbf{s}}_{\mathbf{i1}}$. Fig. 5(b) shows an example of a mode consisting of a linear combination of modes being both axial-symmetric and axi-asymmetric. As stated before, axial-asymmetrical modes are not included in Eq. (21). An example of such a mode, built from a linear combination of modes of this type, is visible in Fig. 5(c). As mentioned at the end of Section 3.1, during the step where the expressions for in-plane fields are solved, an extra DOF $\mathbf{U_t}$ is introduced, which corresponds to the relative axial displacement of the top mass. After coupling to the shaker model, which is described by the two DOFs $\mathbf{U_b}$ and q, the resulting semi-analytical model now in total possesses $15+1+2=18$ DOFs. In this model, only single mode imperfection shapes, i.e. only one $e_i\neq 0$, will be considered.

4. Modal analysis and static buckling analysis

To obtain insight in the eigenfrequencies and damping ratios of the shaker-structure system, modal analyses are performed. Experimental results will be compared with semi-analytical results (using the 18-DOF model with $w_0=0$ m) and for some cases also with FEA results, obtained via the finite element (FE) package MSC.Marc. The used FE model of the complete cylindrical shell consists of 30 000 four-node thin shell elements based on Kirchhoff theory. In MSC.Marc these elements are referred to by element type 139 [22]. The nonlinear kinematic relations used in the FE model are valid for large displacements and moderate rotations. Both in the semi-analytical analysis and in the FEA, the effect of the preload due to the weight of the top mass is taken into account. In order to carry out a modal analysis, both the semi-analytical model and FE model are linearized around the static equilibrium solution.

First, the eigenfrequencies corresponding to the lowest two axi-symmetric modes are determined both experimentally and by using the semi-analytical model. No FEA results are available for these two modes, since the electrical part of the shaker could not be modelled in the FE package. For the experimental approach, frequency response functions (FRFs) are

measured by exciting the system with a randomly varying input voltage E_0, while measuring the relative axial displacement of the top mass $\mathbf{U_t}$. In order to realize a linear response, the excitation level is kept low. The resulting (averaged) FRF shows a heavily damped ($\xi_1 = 0.30$) resonance at $f = f_1 \approx 12$ Hz and a moderately damped ($\xi_2 = 0.05$) resonance at $f = f_2 \approx 182$ Hz, see Fig. 6. The first resonance corresponds to an axial suspension mode of the shaker mass, i.e. a mode dominated by $\mathbf{U_b}$. The second resonance corresponds to an axial suspension mode dominated by $\mathbf{U_t}$, see Fig. 5(a). Based on the experimentally determined damping ratios, the damping parameter of the semi-analytical model c_t (c_{ij} are kept zero, see Eq. (18)) is tuned to fit these ratios. In Fig. 6, also the FRF obtained using the 18-DOF semi-analytical model is depicted. As can be noted, up to f=300 Hz the semi-analytical results are in very good agreement with the experimental results. The measured FRF shows small resonances near f=350 Hz, which are not present in the semi-analytical results. As will be shown next, these resonances are not due to axi-asymmetric modes of the cylindrical shell, since these occur above 850 Hz. In addition, these high-frequency modes only posses weak coupling with the axi-symmetric modes at 12 and 182 Hz, due to imperfections in the shell. Only for very large imperfections (e.g. amplitude 20 times the shell thickness), some very minor influence can be noted in the FRF in the frequency region of the shell eigenfrequencies (i.e. near 1000 Hz). Therefore, the resonances near f=350 Hz are likely due to the finite stiffness of the shaker support structure.

The eigenfrequencies and damping ratios of the lowest axi-asymmetric vibrational eigenmodes of the cylindrical shell, which are also axial-symmetric (see Fig. 5(b)), are experimentally determined for several values of n by exciting the top mass using an impulse hammer. The resulting out-of-plane velocity is measured at height x=L/2, using the laser vibrometer at 40 points, which are distributed equidistantly along the circumference of the shell. Based on these FRFs, the eigenfrequencies with corresponding eigenmodes and damping ratios are determined, see [23] for more details. The experimental results are shown in the 4th and 5th column of Table 3. For n=7 no experimental results are included, since for this value of n no mode could be identified. In Table 3, also *undamped* eigenfrequencies of the *perfect* cylindrical shell structure, determined using the semi-analytical approach (using the 18-DOF model) and using FEA, are shown in, respectively, the 2nd and 3rd column. As can be noted, the semi-analytical results are in good correspondence with the FEA results. The maximum difference is 2 percent for n=4. The semi-analytical results show an average difference of 8 percent with the experimental results. Differences may be due to various reasons, e.g. due to imperfections, which are not accounted for in the semi-analytical and FE model, due to inaccuracies in the identified material properties and/or due to measurement inaccuracies.

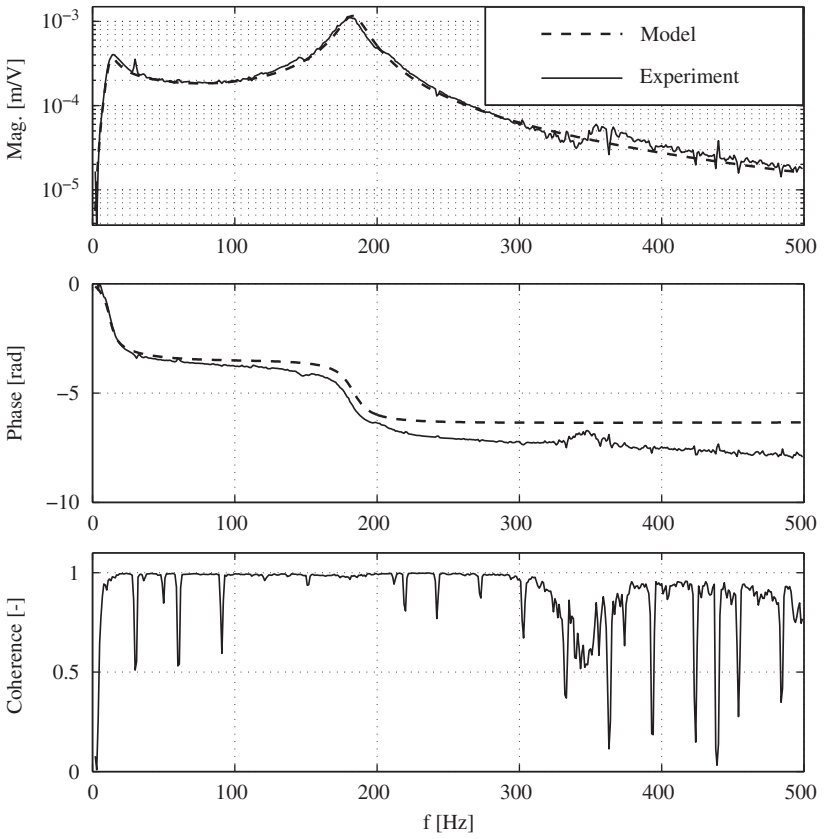

Fig. 6. FRF from input voltage $E_0(t)$ to relative top mass displacement $\mathbf{U_t}(t)$.

Table 3
Eigenfrequencies of lowest axi-asymmetric, axial-symmetric modes; both the 18-DOF and the FE model consider the undamped case for w_0=0 m; ξ_{n1} denotes the experimentally estimated damping ratio.

n	18-DOF (Hz)	FEA (Hz)	Experiment (Hz)	ξ_{n1} (–)
4	1415	1387	1293	0.005
5	1070	1063	1030	0.007
6	896	896	886	0.010
7	858	858	–	–
8	929	926	997	0.020
9	1076	1070	1165	0.010
10	1276	1268	1496	0.007
11	1514	1506	1683	0.020

Next, static buckling of the cylindrical shell is considered. In [24], an analytical expression is derived for the buckling load of orthotropic cylindrical shells with simply supported boundary conditions and being subjected to axial edge loads. If Eq. (29) from [24] is applied, the lowest buckling load for the cylindrical shell under consideration is estimated to be P_c=951 N. The corresponding buckling mode is characterized by n=6 and i=1. Recall that i is the number of half-waves in axial direction, see Eq. (12). However, due to the fact that the cylindrical shell under consideration is mounted between stiff end-rings, its real boundary conditions at both ends of the cylindrical shell are prescribed axial displacements rather than axial edge loads. This difference in the in-plane boundary condition may slightly affect the buckling load and the corresponding buckling mode of moderately long cylindrical shells, to which class the cylindrical shell under consideration belongs [25]. The static buckling of the orthotropic (perfect) shell is also determined using a linearized buckling eigenvalue analysis based on the 18-DOF semi-analytical model and, as a numerical reference, by using FEA based on the same model as used for the modal analysis. Several values of the circumferential wavenumber n are considered. The 18-DOF semi-analytical model predicts the lowest buckling load of the perfect cylindrical shell to be P_c=990 N and the corresponding buckling mode is dominated by n=12 and i=7. The FEA predicts P_c=975 N and a corresponding buckling mode dominated by n=1 and i=9. Note that the buckling mode found by the FEA cannot be predicted accurately by the semi-analytical model, since the adopted shell theory of Donnell is only valid for $n \geq 4$. As is well-known for thin cylindrical shells [25], just above the first critical load, many additional closely spaced buckling loads are obtained. This is confirmed once again by the results obtained above. The buckling loads obtained using the semi-analytical approach and the FEA differ only slightly (2 percent). Based on the buckling load predicted by the FEA, the weight of the top mass, as considered during the experiments, equals 5 percent of the static buckling load, i.e.$m_t \cdot g/P_c = 0.05$ [–].

5. Numerical steady-state analysis

In this section, a numerical steady-state analysis will be performed for the total system consisting of the shaker, the amplifier, and the cylindrical shell with top mass. The objective of this dynamic analysis is to determine, for which combinations of excitation frequency f and amplitude v_d of the input voltage, see Eq. (1)), instabilities occur, and how these results depend on possible geometric imperfections in the cylindrical shell. The amount of damping taken into account during the simulations is based on the experimental modal analysis results as discussed in the previous section, i.e. the damping ratios of the lowest two (axi-symmetric) modes are set to $\xi_1 = 0.3$ and $\xi_2 = 0.05$ (related to c_t and c_b). To all other vibration modes a damping ratio $\xi = 0.01$ is assigned, which is realized via parameters c_{ij}. This value corresponds, more or less, to the average of the experimentally determined damping ratios of the lowest axi-asymmetric modes, see Table 3.

Numerical continuation of periodic solutions [26] in combination with Floquet theory will be used to determine the parameter region(s), where the stability of the harmonic response is lost. In the frequency regions, where the harmonic response is no longer stable, the response is further examined using standard numerical integration and a numerical implementation of a stepped frequency sweep procedure. Detailed results are presented for a circumferential wavenumber n=9, while considering three (single mode) imperfection shapes, i.e. e_1=0.5, e_3=0.5, or e_5=0.5. The influence of the selected value for n will be addressed at the end of this section. The responses of the cylindrical shell are characterized by the following dimensionless measures:

$$u_L = u(t, L, \theta)/L, \tag{22}$$

$$U_m = \max_T u_L - \min_T u_L \geq 0, \tag{23}$$

$$w_{L/2} = w(t, L/2, \pi/(2n))/h, \tag{24}$$

where T=1/f. Note that u_L can be directly computed from the DOF $\mathbf{U_t}$, which was introduced in the model at the end of Section 3.1.

Using numerical continuation of periodic solutions with the excitation frequency f as continuation parameter, it is found that for sufficiently large excitation amplitude v_d, the harmonic response first loses stability in the top of the

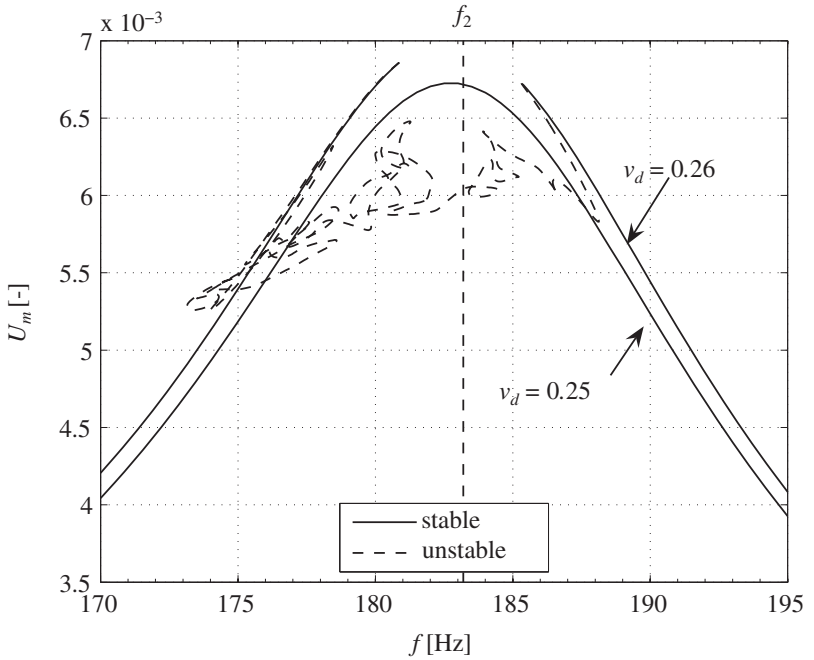

Fig. 7. Frequency–amplitude plot of the imperfect shell (e_1=0.5).

resonance peak near f_2=182 Hz. Recall, that the resonance near f=f_2 corresponds to a vibration mode, which is dominated by axial displacements of the (cylindrical shell with) top mass, i.e. by $\mathbf{U_t}$. Similar to the case of prescribed base-acceleration, discussed in [5], responses with large out-of-plane deflections appear, when the stability of the harmonic solution is lost. The critical value of v_d, for which the harmonic solution loses stability for f=f_2, is called v_d^c.

For the perfect cylindrical shell (w_0=0 m), the harmonic solution loses stability in the peak of the resonance near f=f_2 for $v_d = v_d^c = 0.298$ V. By introducing an imperfection of the form e_1=0.5, this critical value decreases 15 percent to $v_d^c = 0.253$ V. For this case, the frequency–amplitude plots near f=f_2, for v_d just below and just above v_d^c, are depicted in Fig. 7.

As can be noted, for $v_d > v_d^c$, a very complicated branch of unstable periodic solutions appears in the resonance peak near f=f_2, which is initiated by two cyclic fold bifurcations. The response in this region of instability is further examined using standard numerical integration of the equations of motion, see Fig. 8. As can be noted, a beating response appears in the region of instability. Time intervals with small out-of-plane displacements are alternated with time intervals, where the out-of-plane response $w_{L/2}$ of the shell is very severe. In the latter time intervals, very high frequencies can be observed in the transversal acceleration signal $\ddot{w}(L/2)$. In very short time periods associated with these high frequencies, transversal accelerations of the shell up to 20 000g occur. In these very short time periods, these accelerations lead to transversal displacements in the order of the plate thickness, giving rise to nonlinear kinematic coupling between in-plane motion and out-of-plane motion. For these very short time periods, the previous assumption, that the in-plane inertia of the cylindrical shell can be neglected, may become questionable. This may lead to an overestimation of the transversal acceleration. Transversal peak accelerations of the shell surface of 2100g are measured in experiments described in [6] for a more or less comparable structure and situation; in [6], the top mass is free and five times lighter. The power spectral density (PSD) of the beating response is broad-banded (see bottom plot of Fig. 8), suggesting that this response has a chaotic nature.

A possible explaination for the occurring instability phenomenon may be the nonlinear interaction between the axial mode near 182 Hz, see Fig. 5(a), and the shell type of modes present in the high frequency range, i.e. above approximately 850 Hz, see Table 3. Note that the modal density of the shell modes is quite high. The occurring interactions may be caused by direct nonlinear couplings and/or parametric couplings present in the model. As will be shown, the instability phenomenon appears to be robust. It also occurs for other imperfections e_i and other circumferential wavenumbers n.

The response of the total system will be examined experimentally using a stepped sine frequency sweep procedure. The obtained frequency–amplitude plots from these frequency sweep experiments cannot fully be compared with the frequency–amplitude plots computed using the continuation approach, since the latter ones do not include aperiodic responses (as obtained numerically for $v_d > v_d^c$). Therefore, the numerical response is also examined using an implementation of the stepped sine procedure, which is based on numerical integration of the equations of motion. During the stepped sine frequency sweep, the excitation frequency is incrementally increased (in case of sweep-up) or decreased (in case of sweep-down) using a step size $\Delta f = 0.5$ Hz. For each discrete value of f, the signals are saved during N_e=150 excitation periods. The data during the first N_t=50 periods are not used, in order to minimize transient effects.

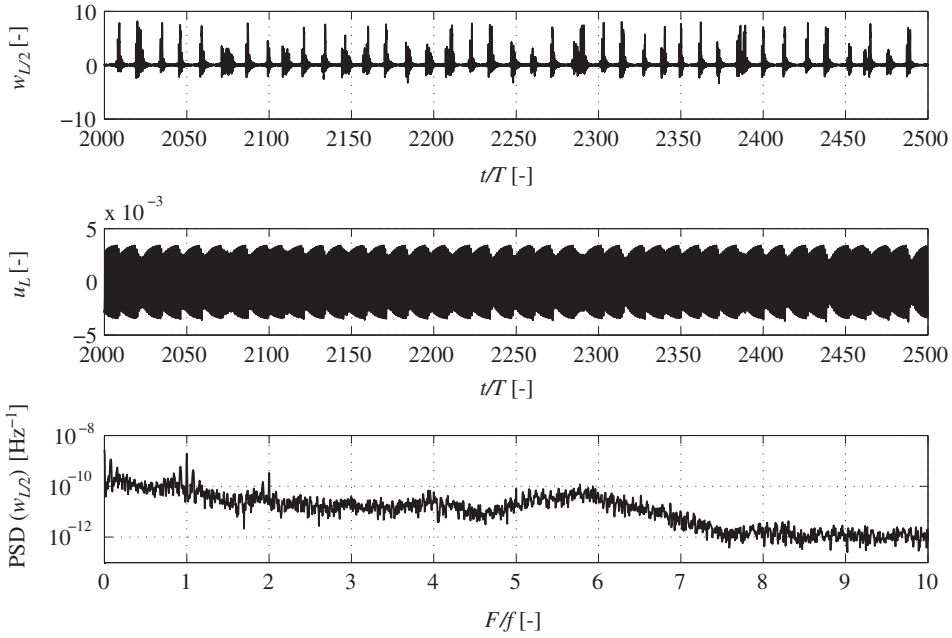

Fig. 8. Response for v_d=0.26 V, f=f_2 and e_1=0.5 [–] in terms of $w_{L/2}$, u_L and the power spectral density of $w_{L/2}$.

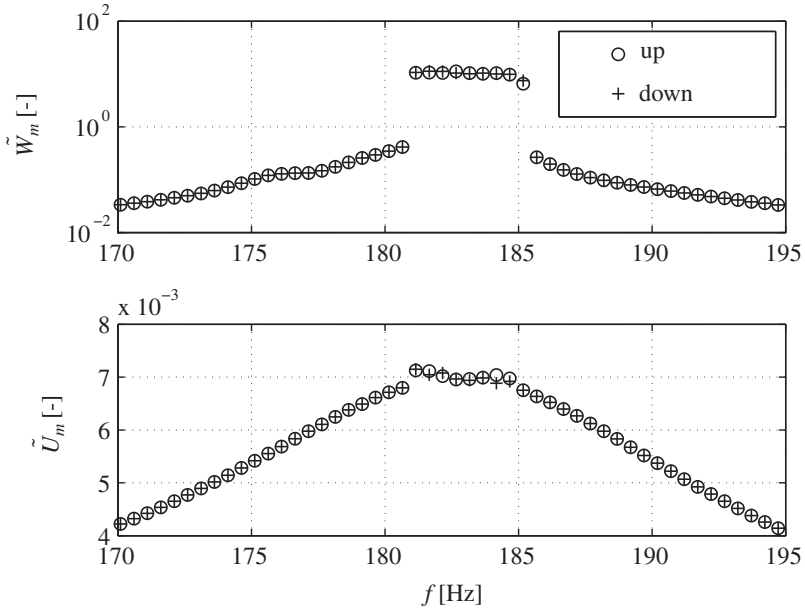

Fig. 9. Frequency–amplitude plot based on frequency sweep analysis for e_1=0.5 and v_d=0.26 V (simulation).

Subsequently, the following averaged response measures are determined:

$$\tilde{U}_m = \frac{1}{N_m}\left(\sum_{k=0}^{N_m-1} \max_{T_m} u_L(t_i+kT_m) - \min_{T_m} u_L(t_i+kT_m)\right), \tag{25}$$

$$\tilde{W}_m = \frac{1}{N_m}\left(\sum_{k=0}^{N_m-1} \max_{T_m} w_{L/2}(t_i+kT_m) - \min_{T_m} w_{L/2}(t_i+kT_m)\right), \tag{26}$$

where $T_m = (N_e - N_t)T/N_m$ and N_m=5 [–]. Note that for harmonic responses, $\tilde{U}_m$ is equivalent with U_m defined by Eq. (23). Time t_i indicates the time at which the i th incremental parameter change takes place. Exactly the same procedure with the same settings for N_e, N_m and N_t will be followed during the experiments.

Results for the numerical frequency sweep for e_1=0.5 and $v_d = 0.26 > v_d^c$ are shown in Fig. 9. Note that $\tilde{W}_m$ is plotted on a logarithmic scale. Very severe out-of-plane responses are suddenly initiated at the boundaries of the region $182 \leq f \leq 185$, where no stable harmonic solutions are found with the continuation approach, see Fig. 7. Note that frequency hysteresis is not observed in Fig. 9.

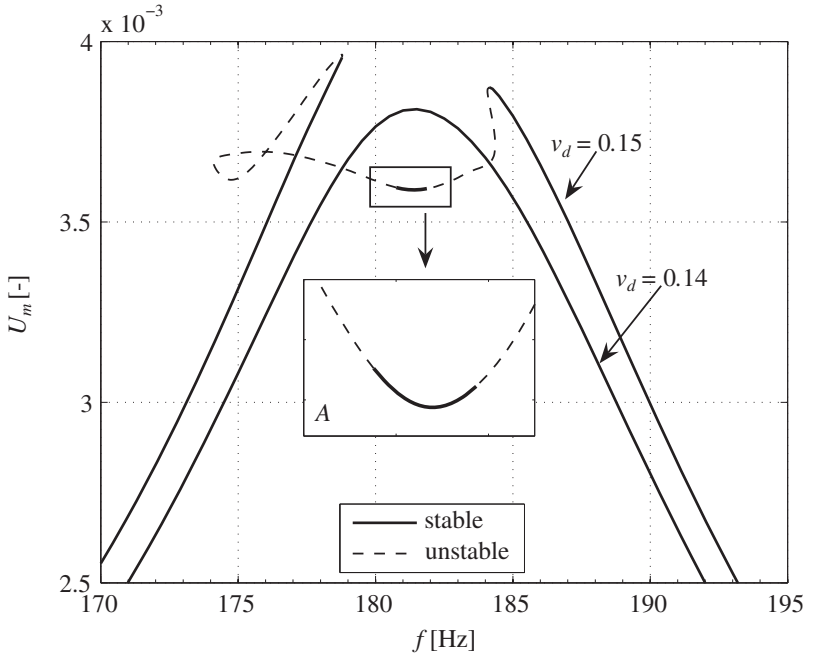

Fig. 10. Frequency–amplitude plot of the imperfect shell (e_3=0.5).

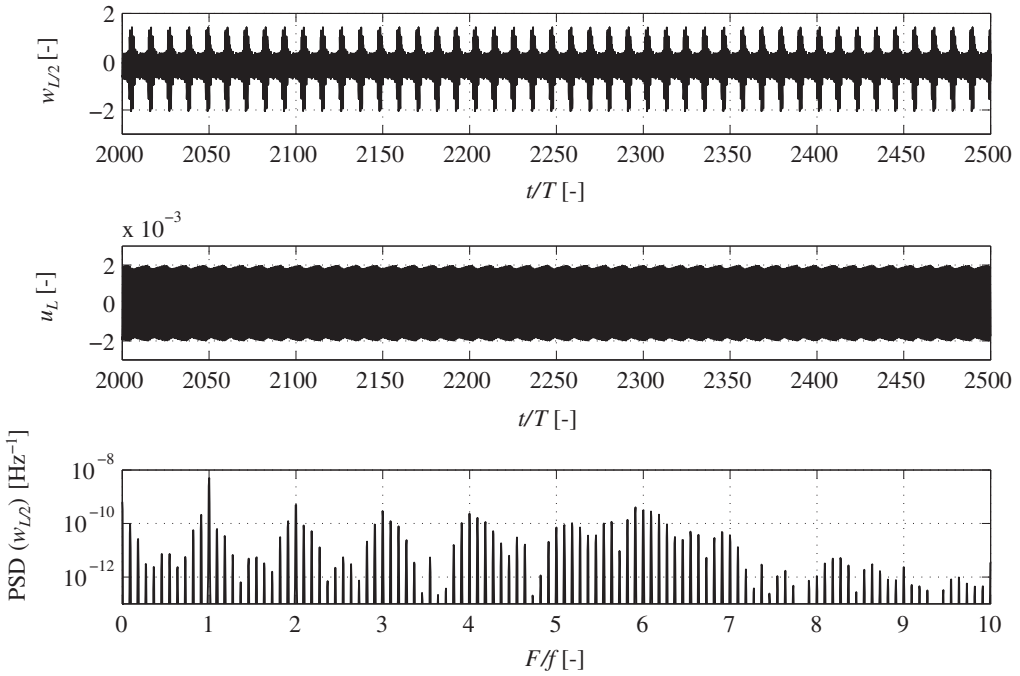

Fig. 11. Response for v_d = 0.15 V, e_3=0.5 and f=183 Hz in terms of $w_{L/2}$, u_L, and the power spectral density of $w_{L/2}$.

Next, an imperfection of the form e_3=0.5 is considered. Using continuation of periodic solutions for this case, a somewhat different scenario is found in the top of the resonance near f=f_2, see Fig. 10. First of all, the harmonic response loses stability at a much lower value of v_d, i.e. $v_d^c = 0.145$ V. Furthermore, for $v_d > v_d^c$ two regions of instability appear. Between these two regions, a small branch with stable harmonic solutions is found, see enlargement A of Fig. 10. An example of the response in the right region of instability at f=183 Hz is depicted in Fig. 11. As can be noted, the PSD of this response shows many discrete peaks, which are equally spaced at $\Delta F/f = 1/11$, suggesting that this beating response is an 1/11 subharmonic response. By plotting T-sampled values of u_L against T-sampled values of $w_{L/2}$, a Poincaré section of this response is constructed, see the right plot of Fig. 13. The Poincaré section shows 11 dots, confirming the 1/11 subharmonic nature of the response. In the left region of instability, a different type of response occurs at f=179 Hz, see Fig. 12. The PSD of this response is broad-banded, suggesting that the response now has a chaotic nature. This suggestion is supported by the fact that the Poincaré map of this response is a bounded cloud of points, see the left plot of Fig. 13. A numerical frequency sweep analysis for e_3=0.5 and $v_d = 0.15 > v_d^c$ [V] reveals that in both regions, where no stable harmonic solutions are obtained, again severe responses appear instead, see the left plots of Fig. 14. As an indication, for the results depicted in Figs. 11 and 12, transversal accelerations in terms of $\ddot{w}(L/2)$ of order 5000g are found. The right plots of Fig. 14 show that for a slightly higher value of the input voltage amplitude (v_d=0.17 V), the region of instability increases in width and also starts to show softening behaviour.

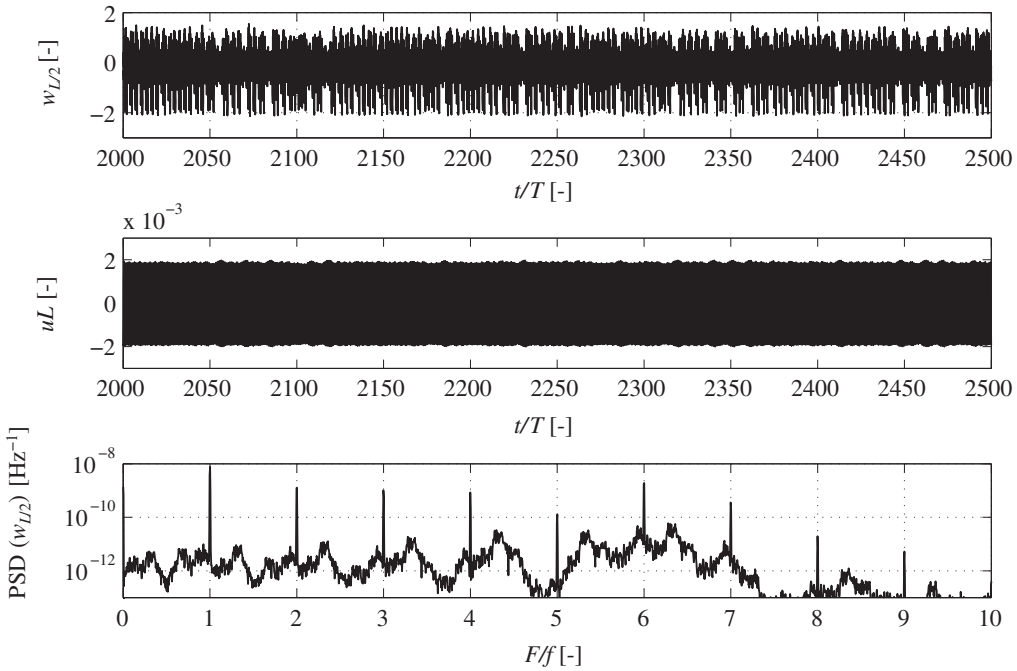

Fig. 12. Response for v_d=0.15 V, e_3=0.5 and f=179 Hz in terms of $w_{L/2}$, u_L, and the power spectral density of $w_{L/2}$.

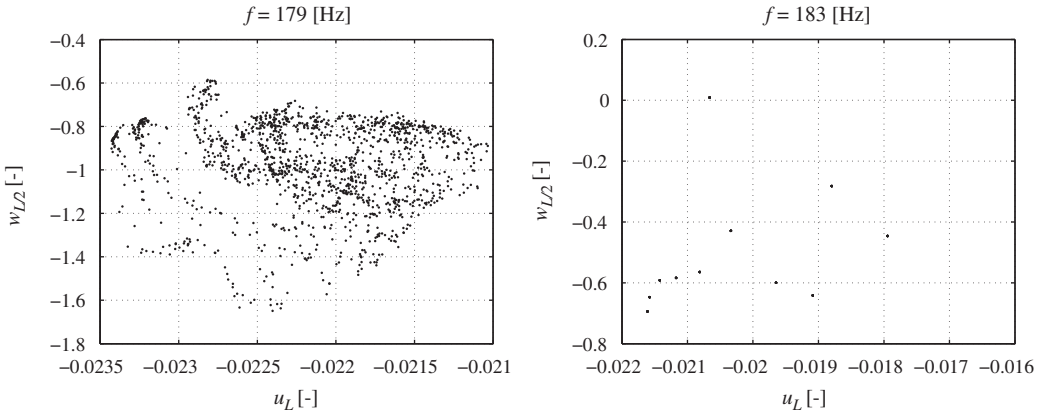

Fig. 13. Poincaré plots of responses shown in Fig. 12 (left) and in Fig. 11 (right).

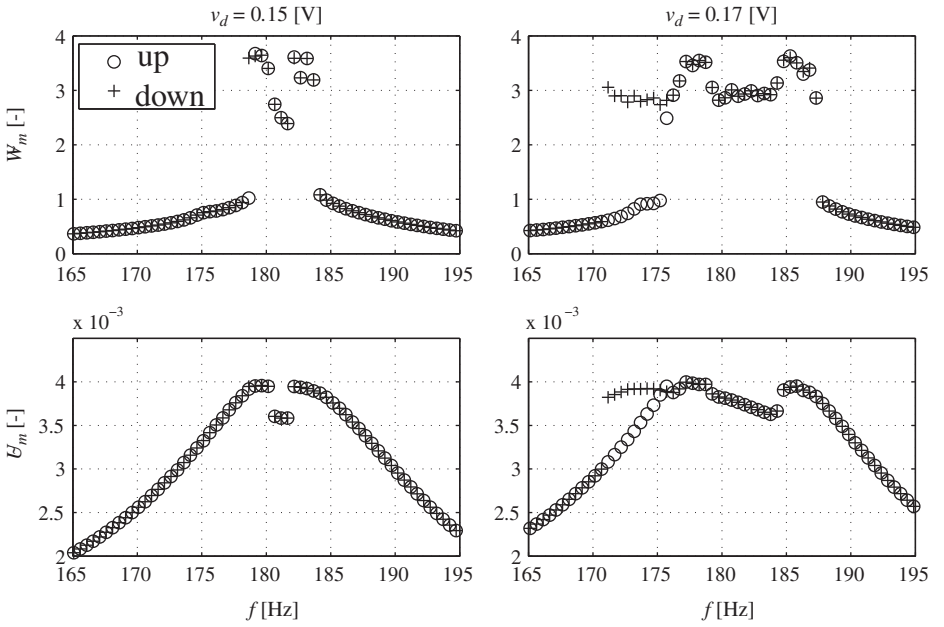

Fig. 14. Frequency–amplitude plots based on frequency sweep analysis for v_d=0.15 V (left) and for v_d=0.17 V (right); in both plots e_3=0.5.

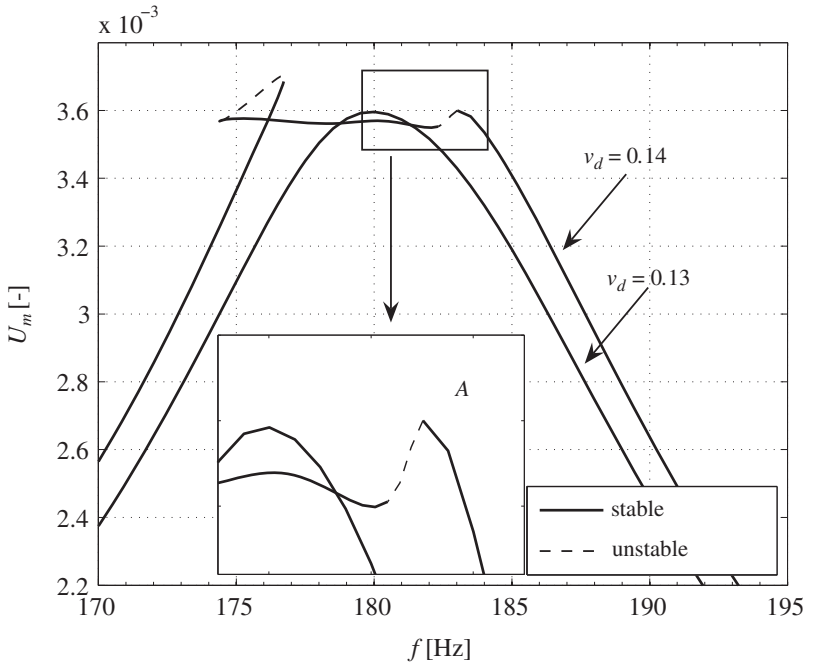

Fig. 15. Frequency–amplitude plot of the imperfect shell (e_5=0.5).

The frequency–amplitude plot for an imperfection of the form e_5=0.5 will be discussed now, see Fig. 15. For this case, the critical amplitude for the input voltage is even lower, i.e. v_d^c=0.135 V. For $v_d > v_d^c$, a region appears on the left hand side of f=f_2, where two stable harmonic solutions coexist. The frequency sweep analysis results for this case are shown in the left plots of Fig. 16. Near f=175 and 183 Hz sudden jumps can be seen in the stepped sine results in terms of $\tilde{W}_m$. One of these jumps occurs in the small frequency region where no stable harmonic solutions exist, see enlargement A in Fig. 15. In this small region, beating responses are found comparable to the response as shown in Fig. 12. For a slightly higher value of v_d (v_d=0.16 V), again the region of instability increases, while the response in terms of $\tilde{W}_m$ significantly increases in amplitude, see the right plots of Fig. 16.

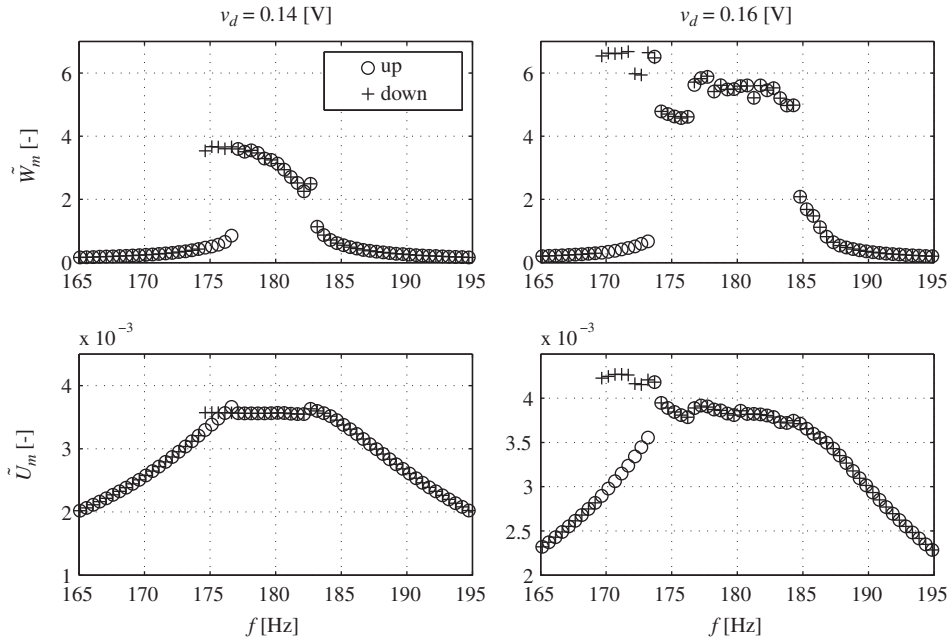

Fig. 16. Frequency–amplitude plots based on frequency sweep analysis for e_5=0.5 and v_d=0.14 V (left) and for v_d=0.16 V (right).

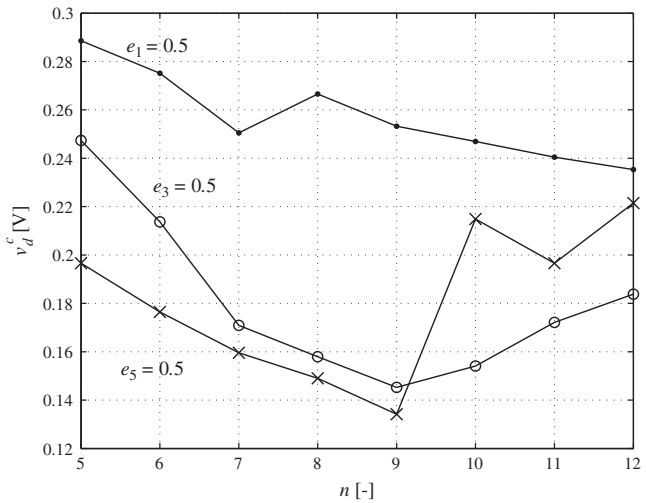

Fig. 17. Influence of circumferential wavenumber n and imperfection e_i on v_d^c.

Finally, the influence of the considered circumferential wavenumber n on the critical amplitude of the input voltage (v_d^c) is examined. In Fig. 17, the influence of n on the value of v_d^c is depicted for three imperfection shapes. For the considered range of n, the lowest value of v_d^c is obtained for n=9 and e_5=0.5, while v_d^c is more than a factor two higher for n=5 and e_1=0.5. This indicates that, similar to the case of prescribed base-acceleration [5], the obtained critical value highly depends on the imperfection shape. Furthermore, also in analogy with the results obtained for the case of prescribed base-acceleration, the lowest obtained critical amplitudes of the input voltage are closely grouped together. As stated before, this may suggest that if one would include additional DOFs to the model corresponding to modes with different circumferential wavenumbers (or perform an experiment on a real cylindrical shell), multiple modes may start to interact for $v_d > v_d^c$, leading to even more complicated dynamics than observed in this section.

6. Experimental steady-state analysis

In this section, experimental results obtained for the shaker excited cylindrical shell with top mass will be discussed. The experimental steady-state results are obtained for a varying excitation frequency and a varying excitation amplitude

using a stepped sine procedure. During the previously presented numerical analyses, $w_{L/2}$ was evaluated at the location, where the largest out-of-plane displacements occurred, see Eq. (24). For the experimental analysis it is unknown, where the largest out-of-plane displacements will occur. Therefore, the angular location for measuring the out-of-plane displacement of the shell is chosen by testing initially a number of angular positions along the circumference of the cylindrical shell at height $x=L/2$, see Fig. 3. The location, where the largest displacements are measured, is used during the actual experiments. The measure $\tilde{U}_m$ is computed using the LVDT measurements, see Fig. 3.

6.1. Results

In Fig. 18, stepped frequency sweep results for various values of v_d and $\Delta f = 0.5$ Hz are depicted. As can be noted, for the smallest considered amplitude of the input voltage (v_d=0.02 V), a single resonance peak appears near f=177 Hz close to

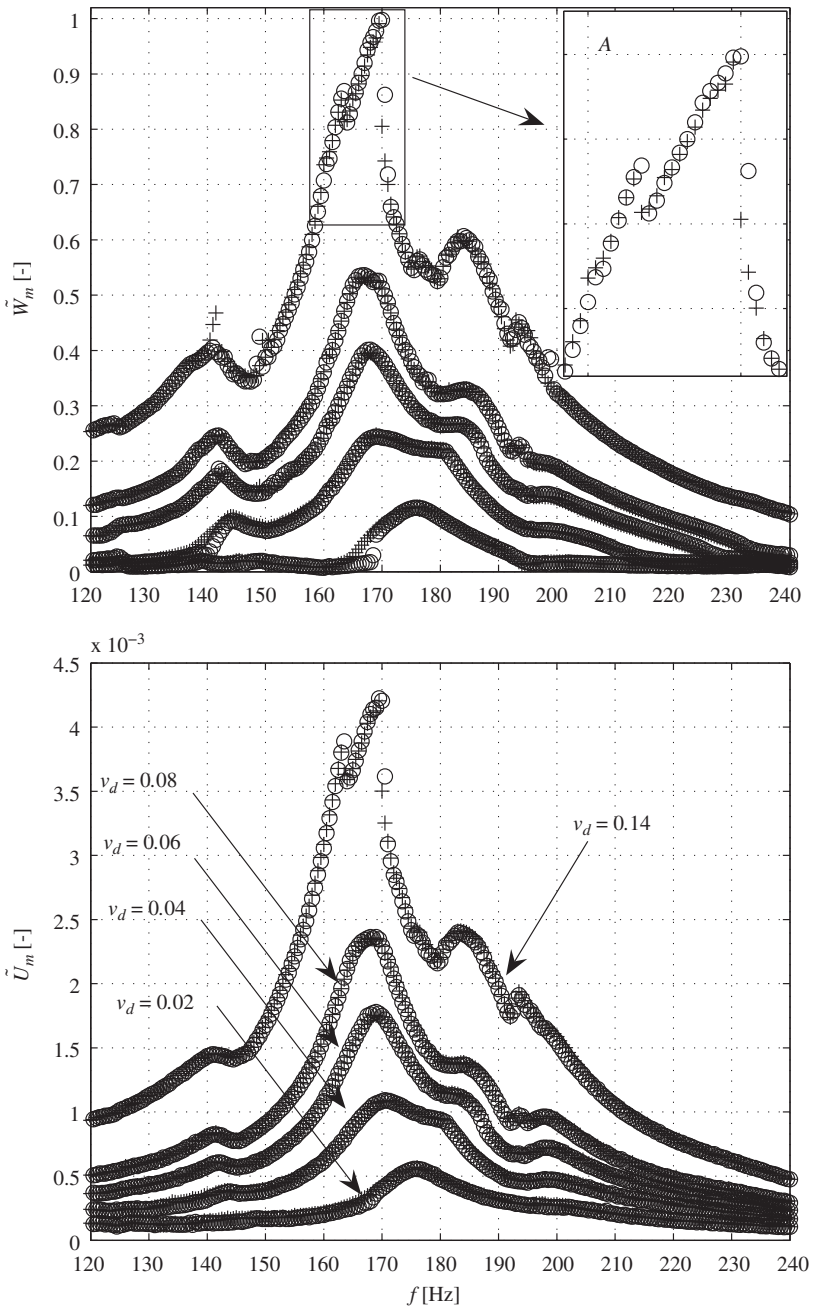

Fig. 18. Frequency sweep results ('+' sweep down, '◦' sweep up).

f_2=182 Hz. By increasing the value of v_d, the amplitude of this resonance peak increases, the resonance frequency decreases somewhat, and additional peaks appear close to this peak. Time histories of the steady-state response for f=170 Hz in terms of $w_{L/2}$ and their PSDs are depicted in Figs. 19 and 20 for, respectively, v_d = 0.06 and 0.08 V. To minimize the effect of measurement noise, each PSD is averaged over eight sets of 2048 data points, measured using a sample frequency of 4 kHz and an anti-aliasing filter. For v_d=0.06 V, the PSD is dominated by peaks at integer multiples of the excitation frequency (F/f=1,2,3,…) indicating a harmonic response. However, for the slightly higher value v_d=0.08 V, additional frequency components appear in the PSD, which exceed the measurement noise level. The time history shown in Fig. 20 seems to be quasi-periodic or slightly chaotic. The transition from the harmonic response to the aperiodic response occurs without a (noticeable) sudden increase in out-of-plane vibrations, i.e. the frequency–amplitude plot does not exhibit jumps for this value of v_d, see Fig. 18.

By increasing the excitation amplitude further to v_d=0.14, the frequency–amplitude plot starts to exhibit jumps near f=162 Hz and near f=170 Hz, see enlargement A in Fig. 18. Especially the jump near f=170 Hz rapidly increases, if v_d is increased even further, see the results for v_d=0.2 V in Fig. 21. Furthermore, several small transition regions can be

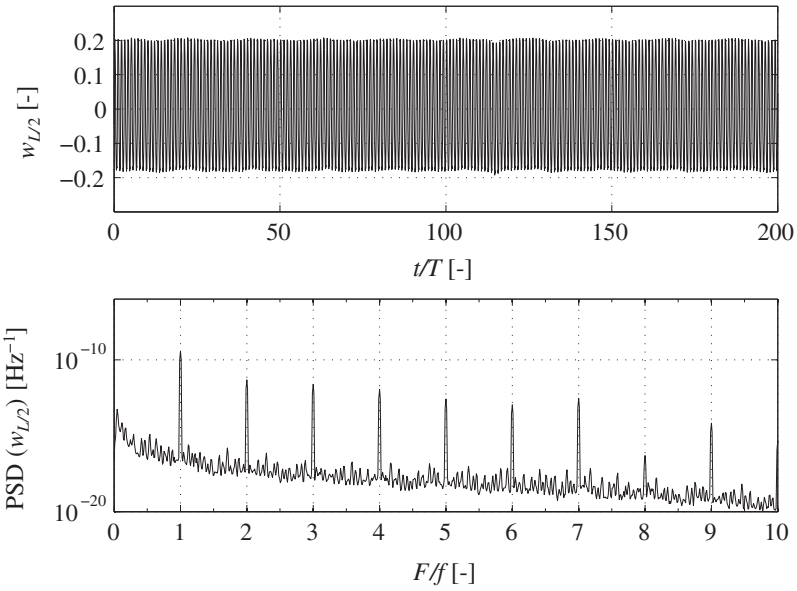

Fig. 19. Measured dimensionless out-of-plane displacement ($w_{L/2}$, top) and corresponding PSD (bottom) for f=170 Hz and v_d=0.06 V.

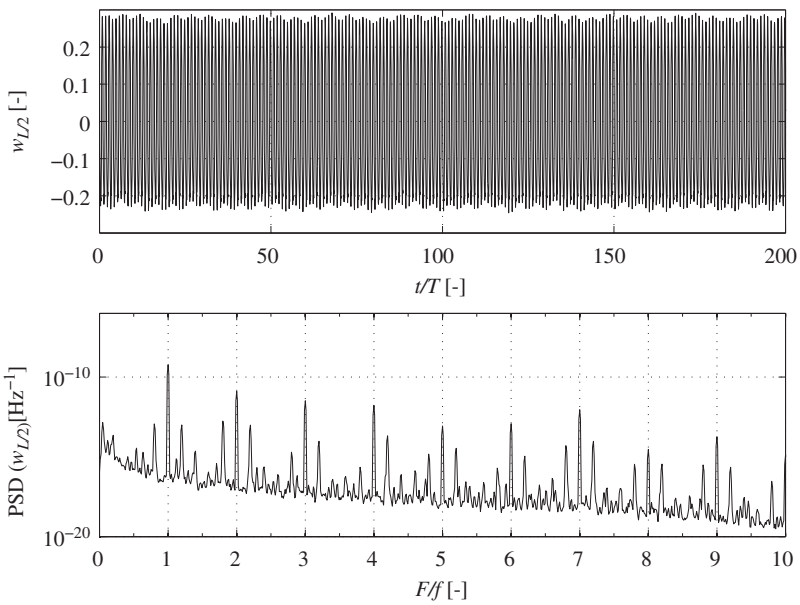

Fig. 20. Measured dimensionless out-of-plane displacement $w_{L/2}$ (top) and corresponding PSD (bottom) for f=170 Hz and v_d=0.08 V.

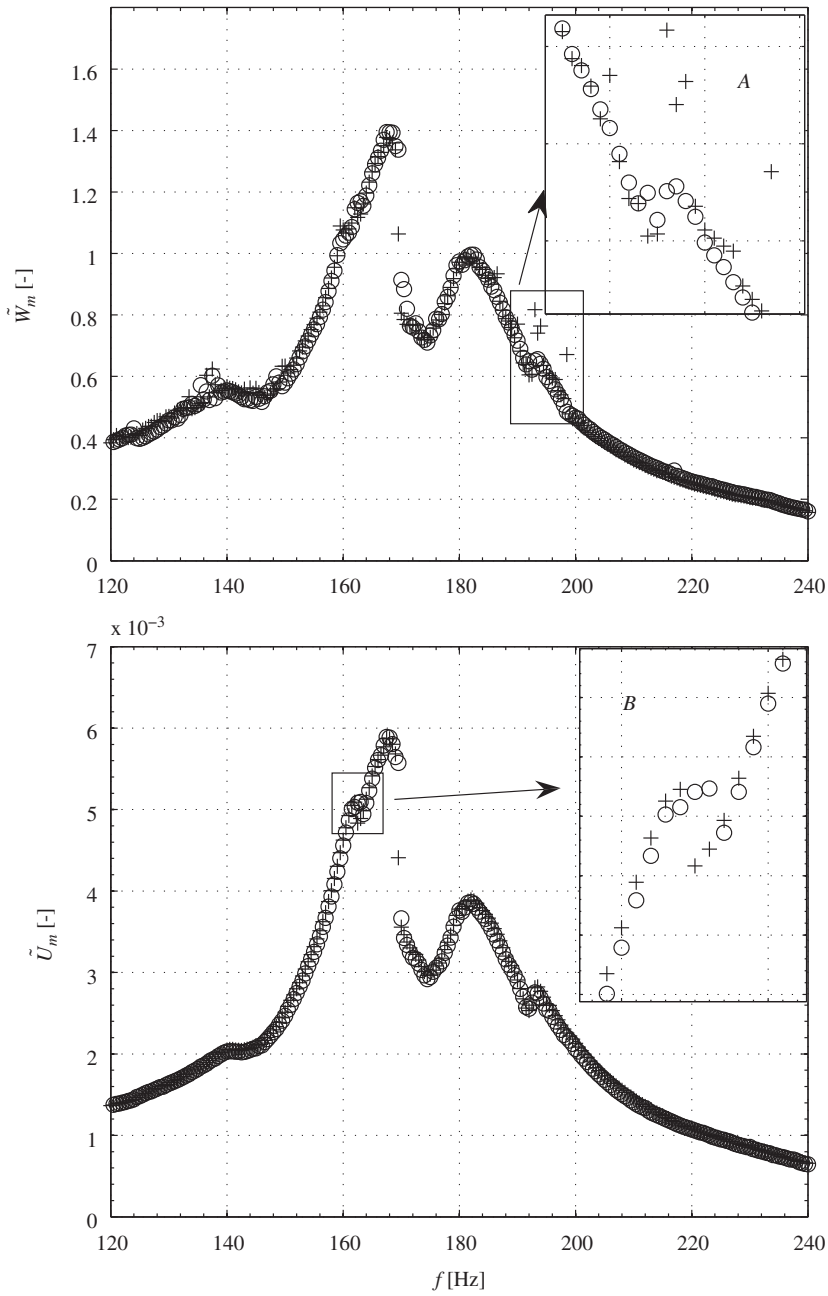

Fig. 21. Frequency sweep results for v_d=0.2 V ('+' sweep down, '∘' sweep up).

observed, see enlargements *A* and *B* in Fig. 21. For this level of v_d, the jump near f=170 Hz can also very clearly be noted audibly. More specifically, for the sweep down, the noise produced by the cylindrical shell suddenly significantly increases after passing the jump. By comparing the time histories of the sweep-down response in terms of $w_{L/2}$ in Fig. 22, i.e. at f=170 Hz just before the large jump, and in Fig. 23, i.e. at f=167.5 Hz just after the large jump, a significant change of the response can be noted. At f=167.5 Hz, the response not only has a much larger amplitude than the response at f=170 Hz, but also has a much broader PSD compared to the PSD measured at f=170 Hz.

6.2. Discussion

Experimentally obtained frequency–amplitude results have been presented for increasing values of the excitation amplitude v_d. Similar as found in the numerical analyses in Section 5, the experiments show a transition from a harmonic

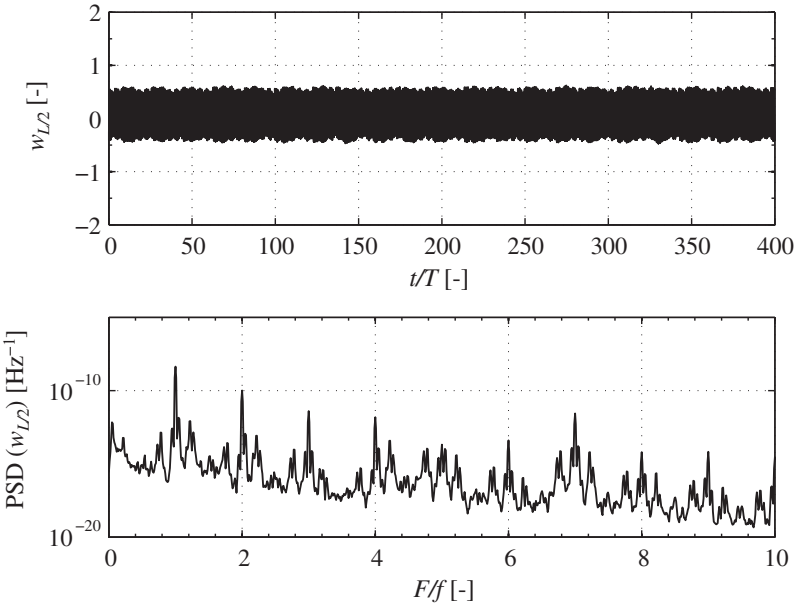

Fig. 22. Measured dimensionless out-of-plane displacement $w_{L/2}$ (top) and corresponding PSD (bottom) for f=170 Hz and v_d=0.20 V.

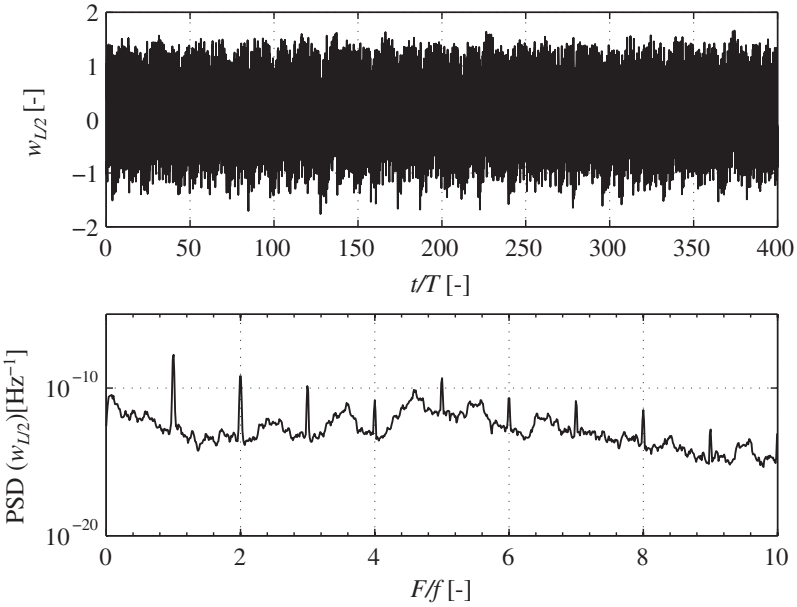

Fig. 23. Measured dimensionless out-of-plane displacement $w_{L/2}$ (top) and corresponding PSD (bottom) for f=167.5 Hz and v_d=0.20 V.

response to an aperiodic large amplitude response near the resonance at $f=f_2$ [Hz]. However, in the experiments for low values of v_d, first additional peaks start to appear near the resonance at $f=f_2$, see Fig. 18. In this frequency region transitions are found, where the response switches from a harmonic response to an aperiodic response, without a (noticeable) sudden increase of the out-of-plane vibrations of the shell. Such behaviour is not found in the semi-analytical analysis. For larger amplitudes of the harmonic input voltage, the experimental frequency–amplitude plot starts to exhibit jumps near f=162 and 170 Hz for $v_d \geq 0.14$ V. By increasing v_d further to $v_d \geq 0.19$ V, large amplitude responses with a very broad PSD appear for excitation frequencies near f=167.5 Hz, see Fig. 23. In the numerical analyses such transitions are found for values of v_d starting near 0.135 V going up to 0.253 V, depending on the shape of the imperfection. Taking into consideration that the critical value for v_d is very sensitive to imperfections, see Section 5, it can be concluded that the transitions to the large amplitude, aperiodic responses in the experiments occur at more or less the same values of v_d, as predicted by the semi-analytical approach.

There may be various reasons for the remaining (quantitative) mismatches between the semi-analytical results and the experimental results. Firstly, the mismatch may be explained by the imperfection sensitivity of the post-critical response as illustrated in the semi-analytical analysis, compare for example Figs. 9, 14, and 16. The cylindrical shell used in the experiments will obviously not be geometrically perfect and its actual (unknown) radial imperfection shape will be different from the imperfection shapes considered in the semi-analytical analysis. Furthermore, at the experimental setup, also other types of imperfections will be present, for example small misalignments between the lower and the upper sledge, see Fig. 3, small thickness variations of the shell and non-perfect shell clamping conditions. As a second cause, arbitrary imperfections in the shell and/or in its boundary conditions will simultaneously trigger multiple axi-asymmetrical modes with different circumferential wavenumbers n. The effect of the participation of multiple modes with different circumferential wavenumbers is not examined in the semi-analytical analysis. However, the effect of variation in the circumferential wavenumber n on the dynamic stability has been considered in the current analysis for several imperfections, see Fig. 17. From these analyses it follows that the lowest obtained critical amplitudes of the input voltage are closely grouped together for different values of n. This suggests that in case of arbitrary imperfections, multiple modes with different circumferential wavenumbers may start to interact for $v_d > v_d^c$. To examine such responses using the semi-analytical approach, more DOFs, corresponding to modes with other circumferential wavenumbers, should be included in the expansion of w and w_0, see Eqs. (12) and (13).

7. Conclusions

The dynamic stability limits of a thin cylindrical orthotropic shell with top mass, which is axially excited at its base by an electrodynamic shaker, are determined both numerically and experimentally. To be able to compare the experimental results with the semi-analytical results, a coupled shaker-structure model is derived. The model is validated firstly by comparing numerical and experimental results for the FRF representing the top mass acceleration response caused by the input voltage, and secondly by comparing experimental eigenfrequencies with eigenfrequencies of linearized models.

The coupled structure exhibits two resonances, which occur at frequencies, which are low compared to resonance frequencies of the cylindrical shell. The first resonance frequency at f_1 [Hz] corresponds to a suspension mode of the shaker mass. The second resonance frequency at f_2 [Hz] corresponds to a suspension mode, which is dominated by axial vibrations of the (cylindrical shell with) top mass. Numerical analyses show that the harmonic response may become unstable near the second resonance frequency and an aperiodic response with severe out-of-plane deformations may appear instead. The critical value for the input voltage, for which the harmonic response changes to the severe post-critical response, highly depends on the initial imperfections present in the shell.

Experiments qualitatively confirm the dynamic response predicted by the semi-analytical model (including the shaker dynamics). Indeed, in the experiments it is shown that, by increasing the excitation amplitude of the harmonic input voltage near the frequency f_2 [Hz], the harmonic response may switch to a severe aperiodic response. A quantitative match between the experimental and the semi-analytical results is not realized yet. In order to achieve this, it is important to extend the semi-analytical model with modes corresponding to multiple circumferential wavenumbers. Moreover, it will be necessary to measure the actual imperfection of the shell under experimental investigation, so that this imperfection can be included in the semi-analytical model.

The presented experimental results confirm the observation from the semi-analytical analysis, that the dynamic stability analysis of base-excited cylindrical shells structures with top mass should be concentrated near a resonance of relatively low frequency, corresponding to an axi-symmetrical suspension mode, dominated by axial vibrations of the (cylindrical shell with) top mass.

References

[1] P. Gonçalves, Z.D. Prado, Nonlinear oscillations and stability of parametrically excited cylindrical shells, *Meccanica* 37 (6) (2002) 569–597.
[2] M. Amabili, M. Païdoussis, Review of studies on geometrically nonlinear vibrations and dynamics of circular cylindrical shells and panels, with and without fluid–structure interaction, *Appl. Mech. Rev.* 56 (4) (2003) 349–356.
[3] E. Jansen, Non-stationary flexural vibration behaviour of a cylindrical shell, *Int. J. Non-Linear Mech.* 37 (4–5) (2002) 937–949.
[4] F. Pellicano, M. Amabili, Stability and vibration of empty and fluid-filled circular shells under static and periodic axial loads, *Int. J. Solids Struct.* 40 (13–14) (2003) 3229–3251.
[5] N. Mallon, R. Fey, H. Nijmeijer, Dynamic stability of a thin cylindrical shell with top mass subjected to harmonic base-acceleration, *Int. J. Solids Struct.* 45 (6) (2008) 1587–1613.
[6] F. Pellicano, Experimental analysis of seismically excited circular cylindrical shells, *Proceedings of the Fifth EUROMECH Nonlinear Dynamics Conference*, Eindhoven, the Netherlands, 2005.
[7] S. Zhang, J. Li, Anisotropic elastic moduli and Poisson's ratios of a poly(ethylene terephthalate) film, *J. Polym. Sci. Part B Polym. Phys.* 42 (3) (2003) 260–266.
[8] N. Mallon, Dynamic Stability of Thin-walled Structures: A Semi-analytical and Experimental Approach, PhD Thesis, Eindhoven University of Technology, 2008.
[9] T. Koga, Effects of boundary conditions on the free vibrations of circular cylindrical shells, *AIAA J.* 26 (11) (1988) 1387–1394.
[10] D. Liu, Nonlinear Vibrations of Imperfect Thin-walled Cylindrical Shells, PhD Thesis, Delft University of Technology, 1988.
[11] M. Amabili, Nonlinear vibrations of circular cylindrical shells with different boundary conditions, *AIAA J.* 41 (6) (2003) 1119–1130.
[12] 〈http://www.tuedacs.nl/〉, TUeDACS Advanced Quadrature Interface.
[13] D. Brush, B. Almroth, *Buckling of Bars, Plates and Shells*, McGraw-Hill, New York, 1975.
[14] L. Donnell, *Beams, Plates and Shells*, McGraw-Hill, New York, 1976.

[15] D.S. Lee, Nonlinear dynamic buckling of orthotropic cylindrical shells subjected to rapidly applied loads, *J. Eng. Math.* 38 (2000) 141–154.
[16] X. Li, Y. Chen, Transient dynamic response analysis of orthotropic circular cylindrical shell under external hydrostatic pressure, *J. Sound Vibr.* 257 (5) (2002) 967–976.
[17] T. Ng, K. Lam, Effects of boundary conditions on the parametric resonance of cylindrical shells under axial loading, *Shock Vibr.* 5 (1998) 343–354.
[18] M. Amabili, Theory and experiments for large-amplitude vibrations of empty and fluid-filled circular cylindrical shells with imperfections, *J. Sound Vibr.* 262 (4) (2003) 921–975.
[19] X. Xu, E. Pavlovskaia, M. Wiercigroch, F. Romeo, S. Lenci, Dynamic interactions between parametric pendulum and electro-dynamical shaker, *Z. Angew. Math. Mech.* 87 (2) (2007) 172–186.
[20] K. McConnell, *Vibration Testing, Theory and Practice*, Wiley, New York, 1995.
[21] A. Preumont, *Mechatronics, Dynamics of Electromechanical and Piezoelectric Systems*, Springer, Berlin, 2006.
[22] MSC.Software corporation, MSC.Marc manual Volume B, Element Library, 2005.
[23] L. den Boer, Modal analysis of a thin cylindrical shell with top mass, Technical Report DCT 2007.086, Eindhoven University of Technology, 2007.
[24] R.D. Zou, C.G. Foster, Simple solution for buckling of orthotropic circular cylindrical shells, *Thin-Walled Struct.* 22 (3) (1995) 143–158.
[25] N. Yamaki, *Elastic Stability of Circular Cylindrical Shells*, Elsevier Science Publishers, Amsterdam, 1987.
[26] E. Doedel, R. Paffenroth, A. Champneys, T. Fairgrieve, Y. Kuznetsov, B. Oldeman, B. Sandstede, X. Wang, AUTO97: Continuation and bifurcation software for ordinary differential equations (with HOMCONT), Technical Report, Concordia University, 1998.